Landsc Ecol
https://doi.org/10.1007/s10980-022-01464-2

RESEARCH ARTICLE

Modelling inter-pixel spatial variation of surface urban heat island intensity

Yanhua Chen · Wendy Y. Chen · Vincenzo Giannico · Raffaele Lafortezza

Received: 24 November 2021 / Accepted: 17 May 2022

Abstract

Context Surface urban heat island intensity (SUHII) is a classical measure depicting urban heat island phenomenon via remotely sensed thermal infrared data. The most common approach is to compare urban and rural land surface temperatures (LST), which is not only sensitive to the selection of pixels/measurements representative of urban and rural areas, but also overlook the pixel-level intra-city SUHII variation and thermodynamics associated with heterogeneous urban landscape.

Objectives This study develops a new $\widehat{\text{SUHIIen}}$, via pixel-based sharpening enhancement method to integrate a pixel's LST magnitude that reflects a city's overall thermal context with its local SUHII that takes the landscape variations and cognate thermal interactions with neighboring pixels into account.

Methods Using Guangzhou (south China) as a case study, $\widehat{\text{SUHIIen}}$ is constructed applying Moderate Resolution Imaging Spectroradiometer LST product for the summer season of 2015 through cloud-based Google Earth Engine platform. The effectiveness of $\widehat{\text{SUHIIen}}$ is tested by comparing $\widehat{\text{SUHIIen}}$ results (based on 3×3, 5×5 and 7×7 kernels) with the original LST, a two-dimensional Gaussian surface, and Gaussian density curve with stepwise increments of the thermal influence from neighboring pixels on the center pixels.

Results We found that (1) local SUHII variations are sensitive to the spatial composition of a center pixel's land use type and that of its eight neighbors; (2) $\widehat{\text{SUHIIen}}$ makes more pronounced those spots that are not only heat per se (with higher original LST), but also receive additional heat load emitted from directly adjacent pixels due to land use homogeneity; (3) the effectiveness of $\widehat{\text{SUHIIen}}$ could be successfully verified.

Conclusions This new SUHI indicator accounts for inter-pixel spatial variation of UHI and highlights how neighboring pixels' homogeneous/heterogeneous land use and associated thermal properties could affect center pixels' thermal characteristics via either reinforcement or mitigation of heat load. It contributes to rigorous assessment of potential heat risks at micro-pixel scale and tailored design of mitigation strategies.

Y. Chen · W. Y. Chen (✉)
Department of Geography, The University of Hong Kong, Pokfulam Road, Hong Kong, China
e-mail: wychen@hku.hk

Y. Chen · W. Y. Chen
International Centre for China Development Studies, The University of Hong Kong, Pokfulam Road, Hong Kong, China

V. Giannico · R. Lafortezza
Department of Agricultural and Environmental Sciences, University of Bari Aldo Moro, Via Amendola 165/A, 70126 Bari, Italy

Published online: 16 June 2022

Keywords Pixel-level sharpening enhancement · MODIS · Inter-pixel thermodynamics · Inter-pixel landscape heterogeneity

Introduction

Urban heat island (UHI) effect denotes higher ambient temperatures in urban environments, as compared with surrounding suburban/rural environments, largely attributing to the thermal energy characteristics of urban surface materials (Oke 1982; Yu et al. 2021a, b). UHI would worsen air quality, increase energy use, and cause heat-related morbidity and mortality (Heaviside et al. 2017). Thus it is regarded as one of the major environmental problems in the twenty-first century facing human society across the globe. Coupled with an increasing concentration of urban population and global warming, the negative impacts of UHI effect are intensifying, which calls for better understanding of the spatially uneven UHI phenomenon in order to identify high-risk spots and incorporate proper urban design for heat risk mitigation (Hulley et al. 2019).

Surface urban heat island intensity (SUHII) is an efficient and reliable way to depict the magnitude and spatial pattern of UHI phenomenon (Stewart and Oke 2012; Zhou et al. 2019). SUHII uses thermal infrared remote sensing data (land surface temperature, LST) derived from multiple airborne or satellite sources to measure the radiative temperature differences between continuous urban and surrounding non-urban surfaces with similar geographic features (Voogt and Oke 2003; Peng et al. 2012; Zhou and Chen 2018), instead of relying on ground-based meteorological monitoring data which are usually spatially scarce and sparsely distributed (Oke 1982; Li and Li 2020). With the advent and rapid advancements of thermal remote sensing technology and easy accessibility to a large corpora of remote sensing data with wall-to-wall coverage of land surface and continuous temporal operation, SUHII has gained increasing attention and wide application in recent decades (Rasul et al. 2017; Zhou and Chen 2018; Li et al. 2020a). It has greatly improved the scientific understanding of UHI phenomenon and associated driving forces (Streutker 2002; Tran et al. 2006; Buyantuyev and Wu 2010), and helped generating useful information for designing anthropogenic interventions to mitigate heat risks in tandem with cognate environmental and public health problems (Jenerette et al. 2016; Deilami et al. 2018; Peng et al. 2020).

The most widely adopted approach for quantifying SUHII is to compare LST differences between urban and surrounding rural areas (Peng et al. 2012; Rasul et al. 2017; Li et al. 2020a). While this measurement could provide simple analytical framework and useful UHI information pertaining to urban vs. rural effects on local climate (Li and Li 2020; Yu et al. 2021a, b), it is sensitive to the selection of representative pixels which can adequately delineate urban and rural areas (Streutker 2002; Deilami et al. 2018; Li et al. 2020a). Moreover, SUHII quantification based on urban–rural comparison commonly views UHI as a constant and uniform phenomenon at coarse scales like the whole urbanized area, and thus tends to ignore micro-scale characters (Yu et al. 2021a) and intra-urban thermodynamics (i.e., heat exchange between warmer to cooler spots) resulted from highly complex biophysical and anthropogenic characteristics (i.e., the interweaving urban fabric of natural spaces and built structures that have marked human transformation of urban landscape and varying levels of anthropogenic heat production in cities) (Rajasekar and Weng 2009; Li et al. 2017; Yu et al. 2021a, b).

To minimize distorted interpretations of SUHII brought by varying urban–rural definitions and investigate the intra-city UHI dynamics, three types of statistical modelling techniques have been proposed. Firstly, Streutker (2002, 2003) and Tran et al. (2006) introduced a two-dimensional Gaussian surface fit model to simulate the multiple features of SUHII, which can generate more UHI information in terms of magnitude and spatiotemporal extents (Anniballe and Bonafoni 2015). However, this model requires a prior extraction of a planar rural background (as a reference with stable thermal inertia) upon which a Gaussian surface can be superimposed to model SUHII spatial dynamics across urban areas (Pereira Filho and Karam 2016; Lai et al. 2021). This technique is suitable for single-center UHI delineation and cannot capture discrete hot spots induced by multi-center urban development patterns (Peng et al. 2020). Secondly, non-parametric kernel convolution model has been proposed (Rajasekar and Weng 2009; Weng et al. 2011), which computes SUHII of each pixel as the difference between the maximum and the mean LST value derived via smoothing center pixel's

LST values together with adjacent pixels. It can capture continuous SUHII over the entire study area, reduce the impact of missing pixels (Keramitsoglou et al. 2011), and avoid biases caused by urban–rural definitions (Zhou and Chen 2018). Nonetheless, this model tends to average the thermal property of center pixel with neighboring pixels, instead of accounting for relevant thermodynamics. Thirdly, linear (parametric) regression function is employed to quantify SUHII via examining the relationship between LST and various metrics of biophysical or socioeconomic factors. These include, but are not limited to, land use and land cover (Li et al. 2012), impervious surface abundance (Yang et al. 2020), normalized difference vegetation index (Sekertekin and Zadbagher 2021), and population density and distribution (Xiao et al. 2008). While regression models can capture the spatial variations of SUHII over various scales from pixel to global through establishing relationships between SUHI and driving factors (Lai et al. 2021), they require a combined input of LST data and related biophysical and socioeconomic data, which might introduce additional uncertainties such as a mismatch of spatial units for LST (e.g., remote sensing gridded pixels) and relevant driving factors (e.g., socioeconomic data based on city blocks or census tracts) (Yin et al. 2018). And these regression models commonly ignore the spatial non-stationary effect of driving factors on SUHI, because they assume that the same predictors (e.g., green spaces) would trigger the same response (LST changes) across the whole study area. In fact, the effect of driving factors on SUHI tends to be spatially varied (Zhao et al. 2018; Li et al. 2020b). Thus, SUHII variations within a whole city might not be adequately captured (Weng et al. 2011; Zhao et al. 2018). While these three types of approaches could delineate pixel-based UHI phenomenon across the urban-periphery-rural continuum, potential inter-pixel thermal exchanges between heat and cold pixels have been largely overlooked, leading to inadequate UHI quantification (i.e., UHI spatial pattern and magnitude) and incomplete pinpointing of urban neighborhoods suffering from higher heat stress that may require immediate mitigation measures and policy attention.

The inherent spatial complexity and heterogeneity of urban surface and associated thermal properties across the whole city creates a limitless array of thermal contexts and microclimate systems (Oke 1982; Buyantuyev and Wu 2010; Weng et al. 2011). For instance, vegetation, building height and density, street canyon morphology, and their spatial arrangement would impact the magnitude and flux of latent and sensible heat exchange (Oke 1982; Di Sabatino et al. 2020), result in substantial intra-city temperature differences, and generate significant intra-city variations of UHI intensity (Zhou et al. 2020). This necessitates site-specific assessment of UHI so that tailored mitigation approaches can be designed (Deilami et al. 2018; Zhao et al. 2018). Therefore, a key issue would be how to use LST at the pixel scale, more importantly, to account for inter-pixel thermodynamics following geographical laws (Wu et al. 2021), to characterize evident intra-city SUHII variations (Weng 2009; Keramitsoglou et al. 2011). In this study, we propose to use a pixel-based sharpening enhancement method to quantify an enhanced SUHII ($\widehat{SUHIIen}$). This new indicator aims to highlight pixel-level SUHII variations across the whole urban area through explicitly accounting for the heating or cooling influences of neighboring pixels on center pixels based on a kernel convolution process. The main objective of this paper therefore is to illustrate the computation of this new indicator and verify its effectiveness via a demonstrative case study using Moderate Resolution Imaging Spectroradiometer (MODIS) land surface temperature data and land use data for Guangzhou (southern China) in the summer season of 2015 using the cloud-based Google Earth Engine (GEE) platform (Gorelick et al. 2017).

Sharpening enhancement approach

Different from the pan-sharpening concept in remote sensing image processing aiming to obtain multi-spectral images of high-resolution by fusing panchromatic images and multi-spectral images (Kwarteng and Chavez 1989; Ma et al. 2020), the sharpening enhancement approach in this study refers specifically to as a technique to detect and enhance the attributes of interest (SUHII in our case study) from a single image source for future processing, i.e. detection, recognition, visualization and analysis. This technique could detect the edge and enhance the image intensity variation by adding the scaled edge information into the spatial domain (instead of homogenization of image intensity), so as to increase the contrast,

explicitly extract the boundary of the image segment, and facilitate the recognition of the target area (Jeevakala 2018). Nonetheless, in line with (Zhan et al. 2013) who defined thermal sharpening as "any procedure through which (remotely sensed) thermal images are enhanced or made clearer for the purpose of interpretation", this study extends beyond this definition of pan-sharpening of thermal images from multiple satellite/aircraft platforms (Duan and Li 2016) to the enhancement of thermal images from one satellite sensor with an aim to highlight the spatial variation of SUHII across the urban-periphery-rural continuum of a study area in avoidance of various uncertainties and tradeoffs amongst different temporal, spatial, and spectral resolutions of images (Zhan et al. 2013; Feng et al. 2015).

To realize sharpening enhancement, many algorithms have been developed in order to highlight the difference, enhance edge information of the image, and differentiate intensity change area in a local context (Torre and Poggio 1986). The first order derivatives, such as Roberts operator (Roberts 1963), Sobel operator (Sobel and Feldman 1968), and Prewitt operator (Prewitt 1970), could filter and detect the magnitude difference of neighboring pixels, and point out the rate and direction of intensity variation. The second order derivatives, such as Laplacian operator or Laplacian of Gaussian (LoG) operator (Marr and Hildreth 1980), Canny operator (Canny 1986), as well as Haralick operator (Haralick 1987), could give stronger responses in finding maximum gradient of intensity changes and isolated points (Dhal et al. 2019). Both Laplacian operator and LoG operator have been widely used for detecting contract between the target pixel and its surrounding (Ratcliffe 1997). Canny operator and Haralick operator are targeted at optimal edge detection using non-maximum suppression and bi-cubic polynomial fitting function, respectively. They tend to focus only on the most significant edges/changes and considerable local information would be neglected.

Besides its wide applications in digital image processing, sharping enhancement technique has been employed to retrieve detailed information from remotely sensed images, such as land surface segmentation and classification (Yu et al. 2018), geological lineament identification (Basu 2002; Han et al. 2018), detection of groundwater zones (Mahmoud and Alazba 2016), reef extraction (Li and Wang 2013), enumeration of olive trees (Waleed et al. 2020), and crop field monitoring (Fu et al. 2008). That being said, the application of sharpening enhancement techniques to characterize SUHII variations across continuous spatial terrains is currently lacking, which promises to reveal more detailed information about SUHI such as boundary and center position, spatial extent, so as to provide tailor-designed planning guideline for mitigating the negative impacts of UHI (Peng et al. 2020).

Methods

The proposed process of $\widehat{SUHIIen}$ quantification is illustrated by Fig. 1. Firstly, sharpening local SUHI variation C[x, y] (local SUHII, the right-hand side of Fig. 1) is computed for each pixel (x, y) with respect to its neighbors within a 3×3 window (the left-hand side of Fig. 1) using Laplacian operator, which detects and quantifies local SUHI variation

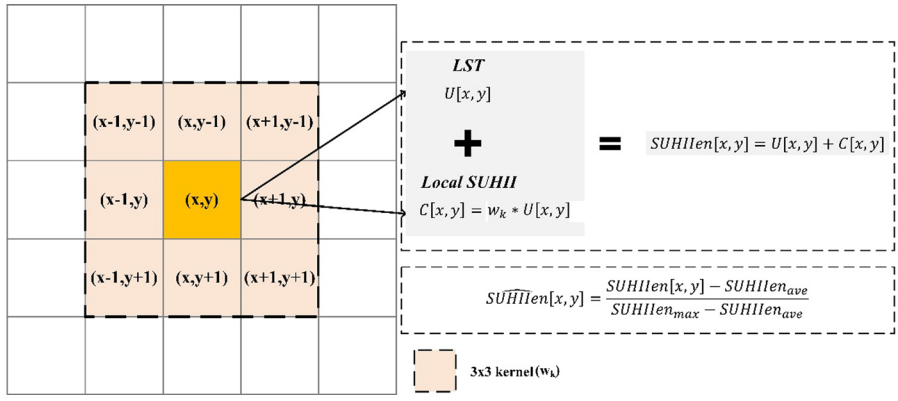

Fig. 1 An overview of the sharpening enhancement method for $\widehat{SUHIIen}$ computation

patterns within this moving window and highlights of the thermal interaction between center pixel and its neighbors. This process is further explained in the following section "Sharpening local SUHII via Laplacian operator". Then the resulted local SUHII C[x, y] is combined with the original LST of each pixel U[x, y] to derive an enhanced SUHII (SUHIIen), and SUHIIen is normalized within the boundary of the city for easy interpretation to obtain $\widehat{SUHIIen}$. More details are given in section "Enhancement of local SUHII: $\widehat{SUHIIen}$".

Sharpening local SUHII via Laplacian operator

Let a digital LST image be U: $\Omega \rightarrow \mathrm{R}$, where $\Omega \subset \mathrm{R}^2$ is image support and the continuous LST image is u. and let the pixel value be $U[x, y]$ at location (x, y) at a specific time. The first derivative is the same as the gradient of the temperature processing in space, which is given as:

$$\nabla u = \left[\frac{\partial u}{\partial x}, \frac{\partial u}{\partial y}\right] \tag{1}$$

where the magnitude of the gradient is given as:

$$|\nabla u| = \sqrt{\left(\frac{\partial u}{\partial x}\right)^2 + \left(\frac{\partial u}{\partial y}\right)^2} \tag{2}$$

and the direction is:

$$\theta = \tan^{-1}\left(\frac{\partial u}{\partial y} \Big/ \frac{\partial u}{\partial x}\right) \tag{3}$$

For image processing, the discrete image of ∇U in Eq. (1) can be calculated by finite-difference approximations of the orthogonal vector x and y. The simple equation for the gradient and direction of a digital image considering the forward difference is shown as follows:

$$\nabla U \approx \left[U[x+1, y] - U[x, y], U[x, y+1] - U[x, y]\right] \tag{4}$$

where the magnitude of the gradient is given by:

$$|\nabla U| = \sqrt{\left(U[x+1, y] - U[x, y]\right)^2 + \left(U[x, y+1] - U[x, y]\right)^2} \tag{5}$$

and the direction is:

$$\theta = \tan^{-1}\frac{U[x, y+1] - U[x, y]}{U[x+1, y] - U[x, y]} \tag{6}$$

The second derivative is the change rate in the first derivative. The Laplacian operator ∇^2, which can also be represented by Δ, of function u is shown as:

$$\nabla^2 u = \frac{\partial^2 u}{\partial x^2} + \frac{\partial^2 u}{\partial y^2} + \frac{\partial^2 u}{\partial x \partial y} + \frac{\partial^2 u}{\partial y \partial x} \tag{7}$$

which has

$$\Delta = \nabla \cdot \nabla \tag{8}$$

While for the first derivative SUHI variation is localized at its maximum or minimum value, for the second derivative it results in the zero (or the passage through zero) and has a positive sign in the zone of ascending ramp and negative in the zone of descending ramp. The second derivative can locate the edge pixels corresponding to the pixel where the rising or falling side of $\nabla^2 u$ passes through the zero (from positive to negative and vice versa), thus detect local SUHI intensity variation.

The second derivative can be approximated by difference equations for the center pixel $U[x, y]$, which is given by:

$$\begin{aligned}\Delta U \approx & \left(U[x+1, y] + U[x-1, y] - 2U[x, y]\right) \\ & + \left(U[x, y+1] + U[x, y-1] - 2U[x, y]\right) \\ & + \left(U[x+1, y+1] + U[x-1, y-1] - 2U[x, y]\right) \\ & + \left(U[x+1, y-1] + U[x-1, y+1] - 2U[x, y]\right) \\ & \approx w_k * U\end{aligned} \tag{9}$$

Local SUHII is quantified considering simultaneously the center pixel U_c and its eight first-order neighboring pixels U_n within moving window through a 3 × 3 Laplacian kernel. w_k is defined as:

$$w_k = \begin{bmatrix} 1/8 & 1/8 & 1/8 \\ 1/8 & -1 & 1/8 \\ 1/8 & 1/8 & 1/8 \end{bmatrix} \tag{10}$$

In this study, only the direct thermal impacts from eight first-order neighbors on the center pixel is considered. We exclude higher-order neighbors (such as second-order and third-order neighbors), mainly due to their indirect thermal impacts on the center pixel.

$C[x, y]$ is used represent the magnitude of local SUHII between the center pixel, U_c, and its neighboring

pixels, U_n, taking into account of the thermal influence exerted by U_n. It is calculated through kernel convolution.

$$C[x,y] = w_k * U[x,y] \tag{11}$$

C[x, y] has three possible results, showing different SUHII patterns and changes.

(1) $C>0$, indicating that neighboring pixels exert a heating impact onto the center pixel within the given window, and the value of C denotes the strength of this heating impact.
(2) $C<0$, indicating that neighboring pixels exert a cooling impact onto the center pixel within the given window, and the value of C denotes the strength of this cooling impact.
(3) $C=0$, showing that there is no SUHII change with the given window, and thus no interactive influence between neighboring and center pixels.

Enhancement of local SUHII: $\widehat{SUHIIen}$

Within the urban boundary, local SUHII is further enhanced to be SUHIIen by adding C variation with U variation which reflect the overall background thermal context, to obtain SUHIIen.

$$SUHIIen[x,y] = U[x,y] + C[x,y] \tag{12}$$

This SUHIIen combines the thermal impacts introduced by neighboring pixels into the center pixel's original LST. It integrates two dimensions of UHI, the original LST (reflecting the overall background context across a city) and local SUHI variation (reflecting the influence of neighboring land use), so as to highlight potential heat/cold islands associated with the land use homogeneity (such as hot centers surrounded by hotter neighbors, and cold centers surrounded by colder neighbors) and moderate heat/cold islands associated with land use heterogeneity (such as hot centers surrounded by cold neighbors, and cold centers surrounded by hot neighbors).

For easy interpretation, a normalized SUHIIen ($\widehat{SUHIIen}$) is computed by

$$\widehat{SUHIIen}[x,y] = \frac{SUHIIen[x,y] - SUHIIen_{ave}}{SUHIIen_{\max} - SUHIIen_{ave}} \tag{13}$$

where $SUHIIen_{max}$ is the maximum value of SUHIIen, and $SUHIIen_{ave}$ is the mean value of SUHIIen across the whole study city. The value of $\widehat{SUHIIen}$ ranges between [− 1, 1]. This $\widehat{SUHIIen}$ can be applied to detect the intensity of UHI and urban cold islands (UCI) at varying scales. And the cloud-based Google Earth Engine (GEE) provides an appropriate platform for executing all computations and visualizing $\widehat{SUHIIen}$ in a timely manner (Gorelick et al. 2017).

An experimental case

Guangzhou city (Fig. 2), located in the Pearl River Delta, southeast China, is selected for a case study to demonstrate the feasibility of $\widehat{SUHIIen}$ and test. Being a typical city experiencing rapid urbanization, its UHI and cognate impacts on citizen's daily life has been of great concern (Chao et al. 2020). Using the standard LST product (MOD11A1) generated by the Moderate Resolution Imaging Spectroradiometer (MODIS) onboard the NASA Terra and Aqua Earth Observation System satellites, $\widehat{SUHIIen}$ is computed on GEE platform and tested using MODIS land use and land cover product (MCD12Q1).

MOD11A1 LST data at 1 km resolution have been verified and extensively used in SUHI studies (Wan et al. 2004; Wang et al. 2008, 2019; Rajasekar and Weng 2009). This LST dataset can maintain sufficient sensitivity to meso-scale urban structures, and thus reflect the intra-city microclimate variations. In this experimental case, daytime (10:30 h local time) observations in the summer season (from June 01 to August 31) of 2015 are selected, as the UHI effect is most pronounced in the summer season and thus requires considerable policy attention (Zhao et al. 2014). Following a recent empirical study (Chakraborty and Lee 2019), two criteria are applied in LST data screening: an average LST error of less than or equal to 3 K, and cloud-free. The seasonal LST is then computed via arithmetically averaging all LST records for each pixel during the study period. This could provide a simple representation of summer LST patterns and also eliminate short term fluctuations in weather and land surface conditions (Li and Dong 2009; Wang et al. 2019).

MCD12Q1 product for 2015 at 500 m resolution is used to test the effectiveness of $\widehat{SUHIIen}$ in depicting pixel-level thermal variations. To match with

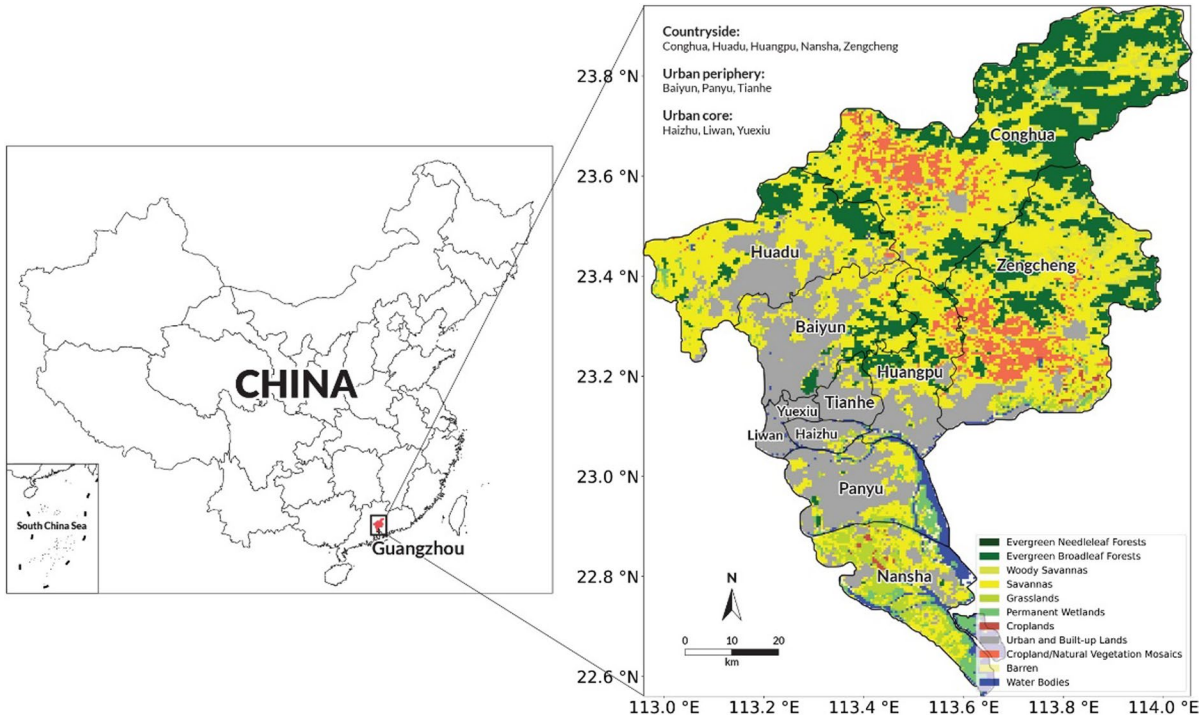

Fig. 2 The study area and land cover of Guangzhou in 2015 with urban core, periphery, and countryside areas delineated by black boundaries

LST data and $\widehat{SUHIIen}$ results, MAC12Q1 product is upscaled to a spatial resolution of 1 km using median aggregation method (Bian and Butler 1999). MAC12Q1 product contains 17 land cover types based on the classification system of the Annual International Geosphere-Biosphere Programme. In Guangzhou, a total of 11 land cover types are finally extracted (Fig. 2). In order to streamline $\widehat{SUHIIen}$ validation, all land cover types are re-grouped into buildings and impervious surface (labeled B: including "urban and built-up land", and "barren land"), green vegetation (labeled G: including "evergreen needleleaf forests", "evergreen broadleaf forests", "woody savannas", "savannas", "grasslands", "permanent wetlands", "croplands", and "cropland/natural vegetation mosaics"), and others (covering "water bodies"). The last group "water bodies" is excluded in our analysis. Four combination patterns can be specified with regard to land cover types of U_c and U_n pixels: (1) vegetation surrounded by buildings (GB), (2) buildings surrounded by vegetation (BG), (3) buildings surrounded by buildings (BB), and (4) vegetation surrounded by vegetation (GG). The Gaussian kernel density fit of $\widehat{SUHIIen}$ for each combination is then plotted to associate computed $\widehat{SUHIIen}$ with land cover patterns, so that the effectiveness of $\widehat{SUHIIen}$ can be verified.

Results

LST, local SUHII, and $\widehat{SUHIIen}$

The original LST, local SUHII variation (intermediate results), and final $\widehat{SUHIIen}$ results are illustrated in Fig. 3. The maximum LST is 40.40 °C, and the minimum LST is 24.64 °C during the summer season of 2015. Clearly, higher LST values are concentrated in Guangzhou's urban core (its old town center including Yuexiu, Liwan, and Haizhu districts) that is mainly covered by dense buildings and impervious surface (shown by grey color in Fig. 2), and LST decreases from urban core toward urban periphery (its suburban districts, including Tianhe, Baiyun, and Panyu districts, with less congested urban

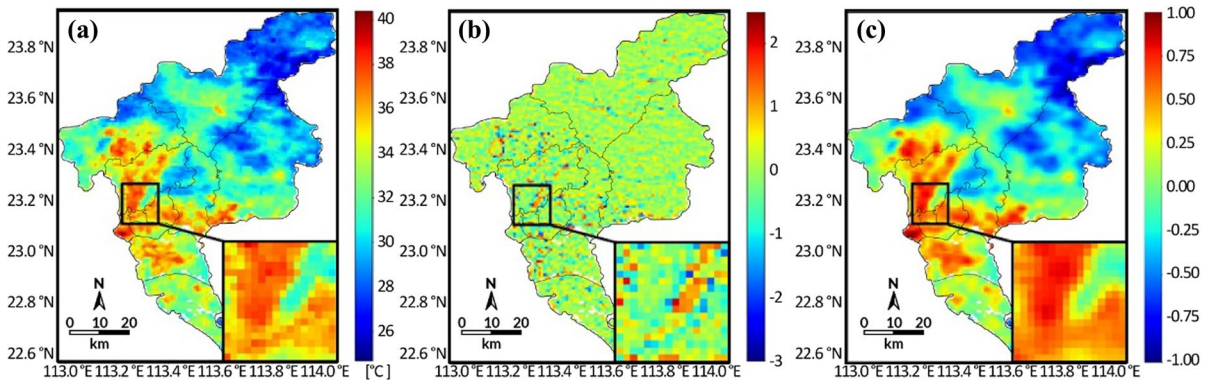

Fig. 3 **a** Original LST, **b** Local SUHII variation, **c** $\widehat{SUHIIen}$, based on a mosaic of MODIS thermal images with a zoomed-in urban core-periphery interface area for more details

development form) and countryside areas (its rural districts, including Huadu, Conghua, Zengcheng, Huangpu and Nansha districts, with only sparse developments in low density) (Fig. 3a) that are largely covered by croplands and various forests (Fig. 2).

When the magnitude of local SUHII variation portrayed by Fig. 3b is considered, significant SUHII variations can be detected across the whole city, shown as red pixels with positive sharpening or blue pixels with negative sharpening, even though a planar SUHII pattern dominates, shown as green pixels with zero SUHII variation. The dominant planar SUHII is resulted from consistent thermal property of land cover between center pixels and their neighboring pixels, while the red and blue pixels reveal neighboring pixels' heating and cooling impacts, respectively. These local SUHII variations are sensitive to the spatial composition and configuration of a center pixel's land cover type and that of its eight neighbors. The significant variation of locally sharpened SUHII reflects the existence of interactive influence within this micro thermal environment (covering a center pixel and its eight neighboring pixels) across the study area resulted from land cover homogeneity (exacerbating UHI or UCI) or heterogeneity (mitigating UHI or UCI). As illustrated by a region containing dense buildings and an urban park (specified by the square in Fig. 3), pixels located at the interface exhibit significant SUHII variations, either negative (displayed with blue tone) or positive (displayed with red tone), resulted from land cover characteristics of their neighboring pixels and their direct influence on ground thermal thermodynamics between the center pixel and its neighbors. For example, abundant vegetation in neighboring pixels would significantly cool down the central pixel that is covered mainly by buildings through thermal conduction and convection (Weng et al. 2004; Deng and Wu 2013; Kim and Guldmann 2014).

Combining this pixel-level SUHI variation with its original LST to generate $\widehat{SUHIIen}$ would therefore successfully retain not only the overall thermal context across the city (as reflected by the original LST), but also capture local variability and interactive mechanisms of inter-pixel thermal patterns. Figure 3c visualizes the estimated $\widehat{SUHIIen}$. A simple visual examination of Fig. 3a and c (retrieved original LST) reveals a similar distribution pattern of UHI. Pixels with negative $\widehat{SUHIIen}$ are mainly found in non-urbanized areas, covered by different types of vegetation. In comparison, pixels with positive $\widehat{SUHIIen}$ are observed inside of urban core areas, which are covered by dense buildings and impervious surfaces. Notably, detailed thermal information reflecting thermal transitions at the boundary separating different land uses can also be found in Fig. 3c, instead of sudden breaks and sharp contrasts between different land surface and thermal properties as portrayed in Fig. 3a. Meanwhile, $\widehat{SUHIIen}$ makes more pronounced some spots that are not only heat per se (with higher original LST), but also receive additional heat load emitted from directly adjacent pixels (when they are hotter than the central pixel, and thus a positive C). Special attention should be paid to these pixels, as more serious health impacts might be triggered for local residents, so that site-specific mitigation strategies

should be formulated. On the contrary, even though some spots are specified as heat islands as indicated by their high LST, their heat load might be moderated via the cooling effect induced by their neighboring pixels (which exhibit significantly lower LST, thus a negative *C*), and thus these spots might not be sites necessitating immediate attention for UHI mitigation.

Verification of $\widehat{SUHIIen}$ using original LST and land use patterns

In addition to simple visual examination and comparison, two measurements (using the original LST and land use patterns) are applied to further validate the effectiveness of computed $\widehat{SUHIIen}$.

Firstly, a simple ordinary least squares regression is used to check the correlation between the original LST and the estimated $\widehat{SUHIIen}$ for each pixel. In this process, three different sizes of the convolution kernel (3×3, 5×5, and 7×7) are adopted to calculate $\widehat{SUHIIen}$ so that the stability of this new indicator across different sizes of the neighbor patch can be detected. The calculated R^2 values are 0.969, 0.936, and 0.905 for the 3×3, 5×5, and 7×7 kernel, respectively. On the one hand, these consistently high R^2 values suggest that $\widehat{SUHIIen}$ is a highly effective indicator applicable for explaining the original LST and cognate UHI phenomenon. On the other hand, these results also reveal the existence of discrepancy between the original LST and $\widehat{SUHIIen}$, attributing to the consideration of neighboring pixel's thermal impacts in $\widehat{SUHIIen}$ computation. Additionally, the R^2 value declines with the expansion of neighbor patch from 3×3 to 7×7. This deviation is anticipated, as the inclusion of the second-order (5×5) and third-order (7×7) neighbors would take additional thermal impacts (from more neighbors) into $\widehat{SUHIIen}$ computation and thus result in stronger difference between $\widehat{SUHIIen}$ and the original LST.

To detect the locational concordance and discordance between the original LST and $\widehat{SUHIIen}$ (based on the 3×3 kernel) in the spatial context of the study area, a bivariate choropleth map is created (Fig. 4). This bivariate map allows for the visualization of two features (LST and $\widehat{SUHIIen}$) in a single map by displaying each feature with a distinct color gradient, whereby the tonally additive result of the overlapping gradients can describe each pixels' degree of concordance or discordance between the LST and $\widehat{SUHIIen}$ (Nöllenburg 2007). In this map, a 9-class sequential color scheme with the LST and $\widehat{SUHIIen}$ being categorized into three classes: low (L), medium (M), and high (H), such that when these two indicators for each pixel are compared, all combination patterns could be reflected using this 9-class sequential color scheme. The cut-off points within each feature are determined using the Jenks natural breaks classification method (Jenks and Caspall 1971), which can minimize each class's average deviation from the class mean and maximize each class's deviation from the means of other classes (Chen et al. 2013).

Overall, the bivariate map showing the spatial concordance between the LST and $\widehat{SUHIIen}$ highlights three distinctive regions (Fig. 4): urban context with high LST and high $\widehat{SUHIIen}$ (HH region), urban periphery with medium LST and medium $\widehat{SUHIIen}$ (MM region), and countryside area with low LST and low $\widehat{SUHIIen}$ (LL region). More importantly, this bivariate map also reveals unequivocally the spatial discordance between the LST and $\widehat{SUHIIen}$, revealing far more complicated micro-thermal situations resulted from pixel-level thermodynamics existing at not only the transitional zones of the urban-periphery-countryside continuum, but also within urban context, periphery zone, as well as rural area. The HL, HM, and ML pixel locations manifest moderating/cooling effect introduced by neighboring pixels, while the LH, LM and MH locations show the reinforcing/heating effect brought by neighboring pixels. The spatially explicit detection of these LST-$\widehat{SUHIIen}$ discordance locations is of pivotal importance, as for these pixels, distorted interpretations of surface urban heat island characteristics would be derived if judging solely based on individual pixels' LST information without taking neighboring pixels' thermal influences into account.

Secondly, based on the classic method proposed by Streutker (2003), a two-dimensional Gaussian surface, which can delineate the area affected by UHI effect and is widely used in UHI studies (Yang et al. 2020; Peng et al. 2020), is obtained using the average LST value of all non-urban land-use classes as the rural background (Schwarz et al. 2011). Figure 5 shows the spatial range of the Gaussian surface and clearly some areas with low LST (Fig. 5a) and with low $\widehat{SUHIIen}$ (Fig. 5b) are included, while some heat areas are excluded. And the correlation between the

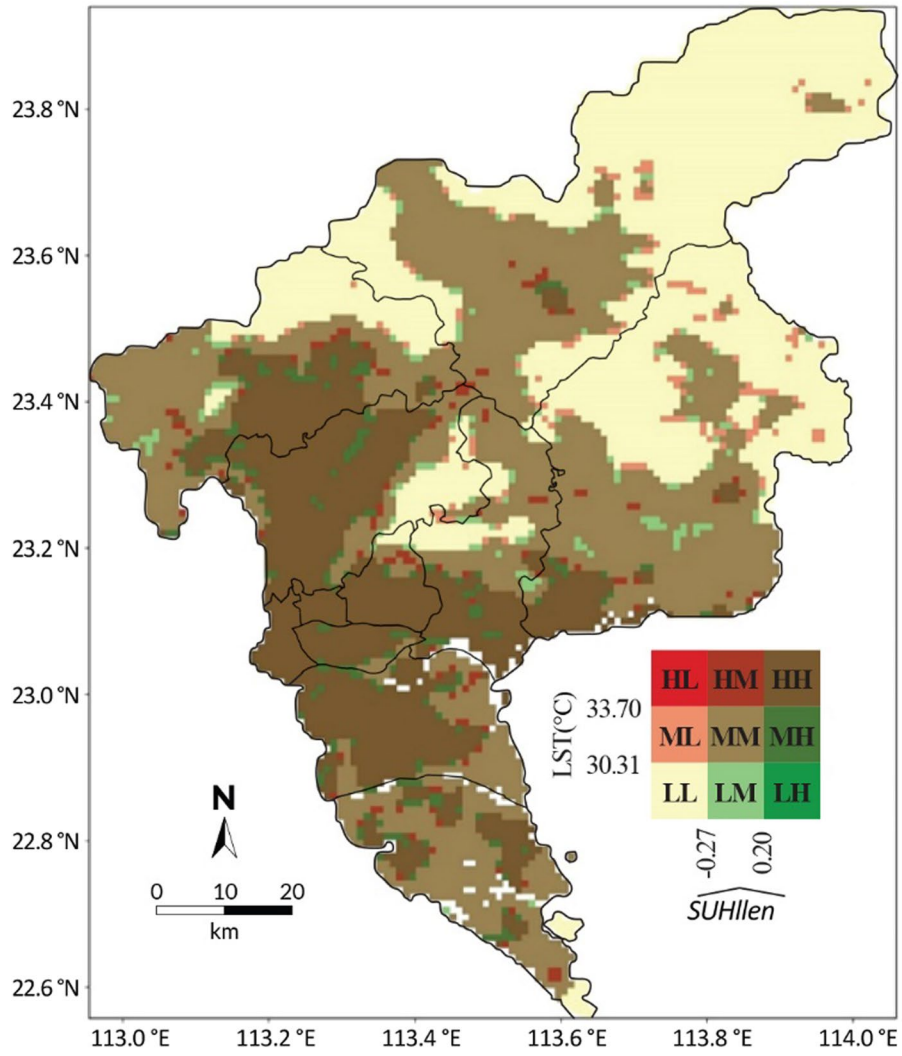

Fig. 4 A 9-class bivariate map showing the concordance/discordance between LST and $\widehat{SUHIIen}$

resulted Gaussian UHI magnitude and the original LST is checked using the ordinary least squares regression, with a result of R^2 at 0.581, suggesting that the Gaussian UHI magnitude could explain about 58% of the original LST variance. As found by Peng et al. (2020), the Gaussian UHI magnitude is more suitable for single-center UHI extraction, which thus cannot adequately capture the UHI pattern when multiple heat centers exist. In comparison, the $\widehat{SUHIIen}$ (based on the 3×3 kernel) could explain 96.9% of the original LST variance, and it is conducive to the study on the spatial pattern of UHI and pinpointing discrete hot spots (with high LST and receiving additional heat impacts from neighboring pixels).

Thirdly, the effectiveness of $\widehat{SUHIIen}$ is further checked with respect to the land use patterns of the center pixel and neighboring pixels, which have been empirically used to interpret SUHII spatial characteristics (Chen et al. 2006; Bokaie et al. 2016; Zhou and Chen 2018). We also plot the distribution of $\widehat{SUHIIen}$ occurrences (Gaussian density curve) for different land use patterns in the study area (Fig. 6). Four typical land use patterns are considered in Fig. 6a, including BB8 (the center pixel with building/imperious surface, surrounded by 8 neighboring pixels with the same building/imperious surface), BG8 (the center pixel with building/imperious surface, surrounded by 8 neighboring pixels with vegetation coverage), GB8 (the center pixel with vegetation coverage, surrounded by 8 neighboring pixels with building/imperious surface) and GG8 (the center pixel with vegetation coverage, surrounded by 8 neighboring pixels

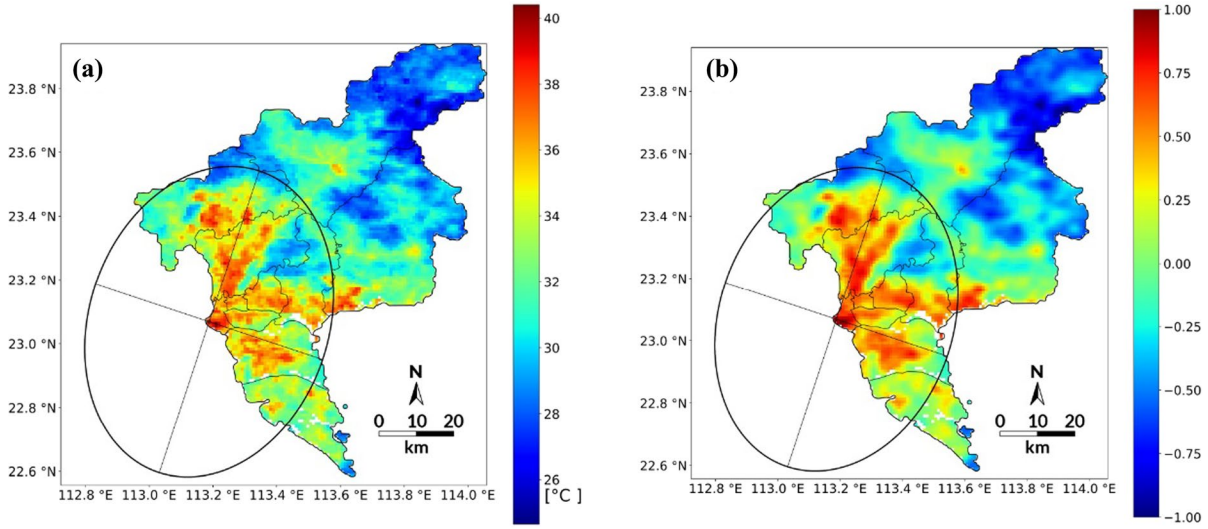

Fig. 5 UHI described by a two-dimensional Gaussian surface, **a** superimposed on the original LST; **b** superimposed on the computed $\widehat{SUHIIen}$ (based on the 3×3 kernel)

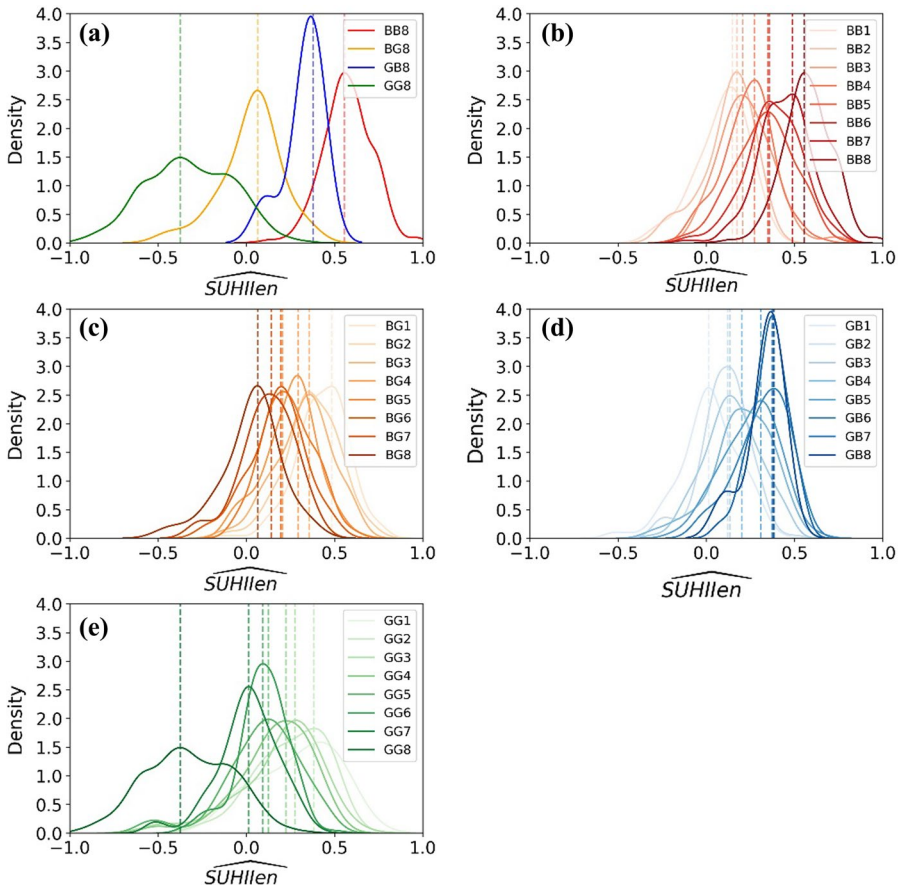

Fig. 6 **a** Gaussian density fit curve of $\widehat{SUHIIen}$ for four typical land use patterns (BB8, BG8, GB8, and GG8). **b–e** Gaussian density fit curve of $\widehat{SUHIIen}$ for the stepwise increments of the thermal influence from neighboring pixels for four typical land use patterns (BB, BG, GB, and GG)

with the same vegetation surface). The peak $\widehat{SUHIIen}$ value (the most probable value) increases from GG8 (− 0.375), to BG8 (0.064), GB8 (0.379), and BB8 (0.556). This trend corroborates that $\widehat{SUHIIen}$ can adequately take into account the thermal properties and interactions between the central and neighboring pixels, as lower $\widehat{SUHIIen}$ values are associated with more vegetation coverage and the cooling effect of this land use type), and higher $\widehat{SUHIIen}$ values are associated with more building and imperious surface and the heating effect of this land use type.

A further step in this verification process is to assess Gaussian density curve with stepwise increments of the thermal influence from neighboring pixels. Figure 6b and 6c illustrate the Gaussian densities for the center pixels with building/imperious surface. Clearly, Fig. 6b reveals that the peak $\widehat{SUHIIen}$ value increases when the number of building-covered neighboring pixels increases from 1 to 8 within the Laplacian kernel, while Fig. 6c shows the peak $\widehat{SUHIIen}$ value decreases, when the number of vegetation-covered neighboring pixels increases from 1 to 8. Similarly, Fig. 6d and 6e illustrate the Gaussian densities for the center pixels with vegetation surface. The peak $\widehat{SUHIIen}$ value increases with an increase of the number of building-covered neighboring pixels (Fig. 6d), decreases with an increase of the number of vegetation-covered neighboring pixels (Fig. 6e). These results imply the heating effect exerted by building/imperious surface and the cooling effect by vegetation in close proximity, thus lend additional support to the effectiveness of the computed $\widehat{SUHIIen}$, even though potential thermal anisotropy associated with land configuration such as building geometry/orientation, urban canyon structure, and vegetation structure/density (Voogt and Oke 2003) that might determine the magnitude of neighboring pixels' thermal influence is not considered in this verification process.

Discussion

Even though LST retrieved from an array of thermal satellite images provides a valuable means to understand UHI phenomenon due to consistent periodicity, high-spatial resolution, and global coverage (Voogt and Oke 2003; Zhou and Chen 2018), how to adequately depict the thermal characteristics and spatial patterns using LST data across the urban-periphery-rural continuum has been challenging and thus exists great room for further development of UHI measurements (Weng et al. 2004; Keramitsoglou et al. 2011; Deng and Wu 2013; Peng et al. 2020; Wu et al. 2021). This paper proposes a new SUHII indicator, $\widehat{SUHIIen}$ (enhanced SUHI intensity), which combines a pixel's original LST that reflects a city's overall thermal context with its thermodynamic characteristics that takes the thermal influence (heating or cooling) of neighboring pixels into account via a pixel-based sharpening enhancement approach. This new indicator could successfully minimize the potential biases brought by urban and rural demarcation, and overcome the limitations of statistical modelling techniques (Keramitsoglou et al. 2011; Zhou and Chen 2018; Yu et al. 2021a, b).

LST is a typical geographical parameter, thus it is necessary to follow geographical laws to adequately describe and consider LST's spatial (and temporal) interactions, i.e., autocorrelation and heterogeneity (Wu et al. 2021). Instead of relying on processing remotely sensed signals only (such as the traditional SUHII indicator derived on the basis of urban–rural LST comparisons which performs well over homogeneous geographic/intra-urban areas without significant land cover changes), $\widehat{SUHIIen}$ embraces Tobler's first law of geography, which states that everything occurring in the realm of space and time is related to everything else, but near things are more related than distant things (Tobler 1970), by accounting for how neighboring pixels' land cover (sharing either homogeneous or heterogeneous features with center pixels) and associated thermal properties could affect center pixels' thermal characteristics via either reinforcement or mitigation of heat load. As highlighted by Wu et al. (2021), this indicator represents a promising approach as it reflects a synthetic integration of geographical law and remotely-sensed data processing technique, so that UHI characteristics across complex geographic areas can be delineated.

The effectiveness of $\widehat{SUHIIen}$ is checked via a demonstrative case in this study using various approaches, including the correlation of with $\widehat{SUHIIen}$ (based on 3×3, 5×5, and 7×7 convolution kernels) with the original LST and a bivariate map showing the spatial concordance between the LST and $\widehat{SUHIIen}$, comparison of $\widehat{SUHIIen}$ with a

two-dimensional Gaussian UHI surface, as well as Gaussian density curve of $\widehat{SUHIIen}$ for different land use patterns (between the center pixel and neighboring pixels). Generally speaking, $\widehat{SUHIIen}$ is able to account for the thermodynamics associated spatial details in land cover homogeneity and heterogeneity, reflect spatial pattern of UHI intensity, and pinpoint hot spots that are not only heat per se (with high original LST) but also receive additional heat load emitted from adjacent pixels thus might have strong threat to inhabitants. This information is of great importance for urban planning and design aiming to mitigate the pressing heat risks. For example, the utilization of green spaces in neighborhoods with high SUHI intensity can effectively avoid the reinforcement of UHI that would lead to stronger negative consequences on energy consumption (for summer cooling) and human health (Yu et al. 2021a, b). While $\widehat{SUHIIen}$ provides a new indicator effectively depicting UHI spatial morphology and enhanced UHI intensity across a whole study area, this study serves as a limited validation, as it cannot yield absolute validation results due to the unavailability of sufficient ground-based in-situ reference measurements.

Conclusion

Different from the original LST or urban–rural LST comparison that have been empirically used to characterize UHI phenomenon (Streutker 2002; Deilami et al. 2018; Li et al. 2020b), this $\widehat{SUHIIen}$ can be computed for the whole urban-periphery-rural continuum, and eliminate the biases caused by the selection of non-representative pixels of urban and rural areas. Additionally, while the conventional SUHII based on urban–rural LST comparison possesses clear physical meaning that explains LST gradient difference between urban and rural areas, $\widehat{SUHIIen}$ is computed via a physically based method thus also with explicit physical meaning. It is able to connote latent thermal interactions at pixel level and specify relatively heat areas ($0 < \widehat{SUHIIen} \leq 1$) and relatively cold areas ($-1 \leq \widehat{SUHIIen} < 0$) as compared with the average condition across the whole city. Thus $\widehat{SUHIIen}$ provides a more in-depth understanding of pixel-level UHI phenomenon across a study area that has complex and heterogeneous land cover and land use, and promises rigorous assessment of potential UHI effects and cognate heat risks.

This $\widehat{SUHIIen}$ can be further expanded into several directions. This study uses only day time LST for summer season to construct and test $\widehat{SUHIIen}$. Therefore it is necessary to check the feasibility and effectiveness of $\widehat{SUHIIen}$ for explaining UHI during night time and different seasons. Moreover, different land use types are grouped into two broad categories in this study, i.e. building/imperious surface, and vegetation. Thus it is not clear how spatial configuration of urban surface structure and land use patterns at finer scales might affect pixel-level thermodynamic properties and also the computation of $\widehat{SUHIIen}$. Furthermore, MODIS data at 1 km resolution is used in this demonstrative case study, whether and how different spatial resolutions of remote sensing data might affect the effectiveness of $\widehat{SUHIIen}$ have not been investigated. In this regard, a $\widehat{SUHIIen}$ adjusted for multiple satellite sensors and more detailed land use patterns might be a promising solution for quantifying SUHI magnitude.

Acknowledgements The authors wish to thank three anonymous reviewers as well as the editor for their helpful comments and suggestions.

Author contributions All authors contributed to the study conception and design. Data collection and analysis were performed by YC. The first draft of the manuscript was written by WYC and YC. All authors commented on previous versions of the manuscript. All authors read and approved the final manuscript.

Funding This work was supported by HKU Foundation Postgraduate Fellowship.

Declarations

Conflict of interest The authors have no relevant financial or non-financial interests to disclose.

References

Anniballe R, Bonafoni S (2015) A stable Gaussian fitting procedure for the parameterization of remote sensed thermal images. Algorithms 8(2):82–91

Basu M (2002) Gaussian-based edge-detection methods—a survey. IEEE Trans Syst Man Cybern C 32(3):252–260

Bian L, Butler R (1999) Comparing effects of aggregation methods on statistical and spatial properties of simulated spatial data. Photogramm Eng Remote Sens 65:73–84

Bokaie M, Zarkesh MK, Arasteh PD, Hosseini A (2016) Assessment of urban heat island based on the relationship between land surface temperature and land use/land cover in Tehran. Sustain Cities Soc 23:94–104

Buyantuyev A, Wu J (2010) Urban heat islands and landscape heterogeneity: linking spatiotemporal variations in surface temperatures to land-cover and socioeconomic patterns. Landsc Ecol 25(1):17–33

Canny J (1986) A computational approach to edge detection. IEEE Trans Pattern Anal Mach Intell 8(6):679–698

Chakraborty T, Lee X (2019) A simplified urban-extent algorithm to characterize surface urban heat islands on a global scale and examine vegetation control on their spatiotemporal variability. Int J Appl Earth Obs Geoinf 74:269–280

Chao L, Huang B, Yuanjian Y, Jones P, Cheng J, Yang Y, Li Q (2020) A new evaluation of the role of urbanization to warming at various spatial scales: evidence from the Guangdong-Hong Kong-Macau region, China. Geophys Res Lett. https://doi.org/10.1029/2020GL089152

Chen X-L, Zhao H-M, Li P-X, Yin Z-Y (2006) Remote sensing image-based analysis of the relationship between urban heat island and land use/cover changes. Remote Sens Environ 104(2):133–146

Chen J, Yang S, Li H, Zhang B, Lv J (2013) Research on geographical environment unit division based on the method of natural breaks (Jenks). In: Proceedings of the ISPRS/IGU/ICA Joint Workshop on borderlands modelling and understanding for global sustainability, Beijing, China, pp 47–50

Deilami K, Kamruzzaman M, Liu Y (2018) Urban heat island effect: a systematic review of spatio-temporal factors, data, methods, and mitigation measures. Int J Appl Earth Obs Geoinf 67:30–42

Deng C, Wu C (2013) Examining the impacts of urban biophysical compositions on surface urban heat island: a spectral unmixing and thermal mixing approach. Remote Sens Environ 131:262–274

Dhal KG, Ray S, Das A, Das S (2019) A survey on nature-inspired optimization algorithms and their application in image enhancement domain. Arch Comput Methods Eng 26(5):1607–1638

Di Sabatino S, Barbano F, Brattich E, Pulvirenti B (2020) The multiple-scale nature of urban heat island and its footprint on air quality in real urban environment. Atmosphere 11(11):1186

Duan S-B, Li Z-L (2016) Spatial downscaling of MODIS land surface temperatures using geographically weighted regression: case study in northern China. IEEE Trans Geosci Remote Sens 54(11):6458–6469

Feng X, Foody G, Aplin P, Gosling SN (2015) Enhancing the spatial resolution of satellite-derived land surface temperature mapping for urban areas. Sustain Cities Soc 19:341–348

Fu S, Ruan Q, Wang W (2008) Remote sensing image data enhancement based on robust inverse diffusion equation for agriculture applications. In: Processing of the 9th international conference on signal procssing, Beijing, China, pp 1231–1234

Gorelick N, Hancher M, Dixon M, Ilyushchenko S, Thau D, Moore R (2017) Google Earth Engine: planetary-scale geospatial analysis for everyone. Remote Sens Environ 202:18–27

Han L, Liu Z, Ning Y, Zhao Z (2018) Extraction and analysis of geological lineaments combining a DEM and remote sensing images from the northern Baoji loess area. Adv Space Res 62(9):2480–2493

Haralick RM (1987) Digital step edges from zero crossing of second directional derivatives. IEEE Trans Pattern Anal Mach Intell 6(1):58–68

Heaviside C, Macintyre H, Vardoulakis S (2017) The urban heat island: implications for health in a changing environment. Curr Environ Health Rep 4(3):296–305

Hulley G, Shivers S, Wetherley E, Cudd R (2019) New ECOSTRESS and MODIS land surface temperature data reveal fine-scale heat vulnerability in cities: a case study for Los Angeles County, California. Remote Sens 11(18):2136

Jeevakala S (2018) Sharpening enhancement technique for MR images to enhance the segmentation. Biomed Signal Process Control 41:21–30

Jenerette GD, Harlan SL, Buyantuev A, Stefanov WL, Declet-Barreto J, Ruddell BL, Myint SW, Kaplan S, Li X (2016) Micro-scale urban surface temperatures are related to land-cover features and residential heat related health impacts in Phoenix, AZ, USA. Landsc Ecol 31(4):745–760

Jenks GF, Caspall FC (1971) Error on choroplethic maps: definition, measurement, reduction. Ann Assoc Am Geogr 61(2):217–244

Keramitsoglou I, Kiranoudis CT, Ceriola G, Weng Q, Rajasekar U (2011) Identification and analysis of urban surface temperature patterns in Greater Athens, Greece, using MODIS imagery. Remote Sens Environ 115(12):3080–3090

Kim J-P, Guldmann J-M (2014) Land-use planning and the urban heat island. Environ Plan B 41(6):1077–1099

Kwarteng P, Chavez A (1989) Extracting spectral contrast in Landsat Thematic Mapper image data using selective principal component analysis. Photogramm Eng Remote Sens 55(1):339–348

Lai J, Zhan W, Voogt J, Quan J, Huang F, Zhou J, Bechtel B, Hu L, Wang K, Cao C, Lee X (2021) Meteorological controls on daily variations of nighttime surface urban heat islands. Remote Sens Environ 253:112198

Li Q, Dong W (2009) Detection and adjustment of undocumented discontinuities in Chinese temperature series using a composite approach. Adv Atmos Sci 26(1):143–153

Li N, Li X (2020) The impact of building thermal anisotropy on surface urban heat island intensity estimation: an observational case study in Beijing. IEEE Geosci Remote Sens Lett 17(12):2030–2034

Li G, Wang Q (2013) Research on reefs extraction method based on multi-spectral remote sensing. In: Proceedings of the 6th international conference on business intelligence and financial engineering, Hangzhou, China, pp 14–17

Li Y-y, Zhang H, Kainz W (2012) Monitoring patterns of urban heat islands of the fast-growing Shanghai metropolis, China: using time-series of Landsat TM/ETM+ data. Int J Appl Earth Obs Geoinf 19:127–138

Li W, Cao Q, Lang K, Wu J (2017) Linking potential heat source and sink to urban heat island: heterogeneous

effects of landscape pattern on land surface temperature. Sci Total Environ 586:457–465
Li J, Wang F, Fu Y, Guo B, Zhao Y, Yu H (2020a) A novel SUHI referenced estimation method for multicenters urban agglomeration using DMSP/OLS nighttime light data. IEEE J Sel Top Appl Earth Obs Remote Sens 13:1416–1425
Li L, Zha Y, Zhang J (2020b) Spatially non-stationary effect of underlying driving factors on surface urban heat islands in global major cities. Int J Appl Earth Obs Geoinf 90:102131
Ma J, Yu W, Chen C, Liang P, Guo X, Jiang J (2020) Pan-GAN: an unsupervised pan-sharpening method for remote sensing image fusion. Inf Fusion 62:110–120
Mahmoud SH, Alazba AA (2016) Integrated remote sensing and GIS-based approach for deciphering groundwater potential zones in the central region of Saudi Arabia. Environ Earth Sci 75(4):344
Marr D, Hildreth E (1980) Theory of edge detection. Proc R Soc Lond Ser B Biol Sci 207(1167):187–217
Nöllenburg M (2007) Geographic visualization. In: Kerren A, Ebert A, Meyer J (eds) Human-centered visualization environments. Springer, Berlin, pp 257–294
Oke TR (1982) The energetic basis of the urban heat island. Q J R Meteorol Soc 108(455):1–24
Peng S, Piao S, Ciais P, Friedlingstein P, Ottle C, Bréon F-M, Nan H, Zhou L, Mynen RB (2012) Surface urban heat island across 419 global big cities. Environ Sci Technol 46(2):696–703
Peng J, Hu Y, Dong J, Liu Q, Liu Y (2020) Quantifying spatial morphology and connectivity of urban heat islands in a megacity: a radius approach. Sci Total Environ 714:136792
Pereira Filho AJ, Karam HA (2016) Estimation of long term low resolution surface urban heat island intensities for tropical cities using MODIS remote sensing data. Urban Climate 17:32–66
Prewitt JMS (1970) Object enhancement and extraction. Pict Process Psychopict 10(1):15–19
Rajasekar U, Weng Q (2009) Urban heat island monitoring and analysis using a non-parametric model: a case study of Indianapolis. ISPRS J Photogramm Remote Sens 64(1):86–96
Rasul A, Balzter H, Smith C, Remedios J, Adamu B, Sobrino JA, Srivanit M, Weng Q (2017) A review on remote sensing of urban heat and cool islands. Land 6(2):38
Ratcliffe CP (1997) Damage detection using a modified Laplacian operator on mode shape data. J Sound Vib 204(3):505–517
Roberts LG (1963) Machine perception of three-dimensional solids. Doctoral Dissertation, Massachusetts Institute of Technology
Schwarz N, Lautenbach S, Seppelt R (2011) Exploring indicators for quantifying surface urban heat islands of European cities with MODIS land surface temperatures. Remote Sens Environ 115(12):3175–3186
Sekertekin A, Zadbagher E (2021) Simulation of future land surface temperature distribution and evaluating surface urban heat island based on impervious surface area. Ecol Ind 122:107230
Sobel I, Feldman G (1968) A 3 × 3 isotropic gradient operator for image processing. A talk at the Stanford Artificial Project
Stewart ID, Oke TR (2012) Local climate zones for urban temperature studies. Bull Am Meteorol Soc 93(12):1879–1900
Streutker DR (2002) A remote sensing study of the urban heat island of Houston, Texas. Int J Remote Sens 23(13):2595–2608
Streutker DR (2003) Satellite-measured growth of the urban heat island of Houston, Texas. Remote Sens Environ 85(3):282–289
Tobler WR (1970) A computer movie simulating urban growth in the Detroit region. Econ Geogr 46:234–240
Torre V, Poggio TA (1986) On edge detection. IEEE Trans Pattern Anal Mach Intell. https://doi.org/10.1109/TPAMI.1986.4767769
Tran H, Uchihama D, Ochi S, Yasuoka Y (2006) Assessment with satellite data of the urban heat island effects in Asian mega cities. Int J Appl Earth Obs Geoinf 8(1):34–48
Voogt JA, Oke TR (2003) Thermal remote sensing of urban climates. Remote Sens Environ 86(3):370–384
Waleed M, Um T-W, Khan A, Ahmad Z (2020) An automated method for detection and enumeration of olive trees through remote sensing. IEEE Access 8:108592–108601
Wan Z, Zhang Y, Zhang Q, Li ZL (2004) Quality assessment and validation of the MODIS global land surface temperature. Int J Remote Sens 25(1):261–274
Wang W, Liang S, Meyers T (2008) Validating MODIS land surface temperature products using long-term nighttime ground measurements. Remote Sens Environ 112(3):623–635
Wang R, Cai M, Ren C, Bechtel B, Xu Y, Ng E (2019) Detecting multi-temporal land cover change and land surface temperature in Pearl River Delta by adopting local climate zone. Urban Climate 28:100455
Weng Q (2009) Thermal infrared remote sensing for urban climate and environmental studies: methods, applications, and trends. ISPRS J Photogramm Remote Sens 64(4):335–344
Weng Q, Lu D, Schubring J (2004) Estimation of land surface temperature–vegetation abundance relationship for urban heat island studies. Remote Sens Environ 89(4):467–483
Weng Q, Rajasekar U, Hu X (2011) Modeling urban heat islands and their relationship with impervious surface and vegetation abundance by using ASTER images. IEEE Trans Geosci Remote Sens 49(10):4080–4089
Wu P, Yin Z, Zeng C, Duan S-B, Göttsche F-M, Ma X, Li X, Yang H, Shen H (2021) Spatially continuous and high-resolution land surface temperature product generation: a review of reconstruction and spatiotemporal fusion techniques. IEEE Geosci Remote Sens Mag 9:112–137
Xiao R, Weng Q, Ouyang Z, Li W, Schienke EW, Zhang Z (2008) Land surface temperature variation and major factors in Beijing, China. Photogramm Eng Remote Sens 74(4):451–461
Yang Z, Witharana C, Hurd J, Wang K, Hao R, Tong S (2020) Using Landsat 8 data to compare percent impervious surface area and normalized difference vegetation index as indicators of urban heat island effects in Connecticut, USA. Environ Earth Sci 79(18):1–13

Yin C, Yuan M, Lu Y, Huang Y, Liu Y (2018) Effects of urban form on the urban heat island effect based on spatial regression model. Sci Total Environ 634:696–704

Yu R, Fu X, Jiang H, Wang C, Li X, Zhao M, Ying X, Chen H (2018) Remote sensing image segmentation by combining feature enhanced with fully convolutional network. In: Cheng L, Leung A, Ozawa S (eds) Neural information processing. Springer, Cham, pp 406–415

Yu Z, Jing Y, Yang G, Sun R (2021a) A new urban functional zone-based climate zoning system for urban temperature study. Remote Sens 13:251

Yu Z, Fryd O, Sun R, Jørgensen G, Yang G, Özdil NC, Vejre H (2021b) Where and how to cool? An idealized urban thermal security pattern model. Landsc Ecol 36(7):2165–2174

Zhan W, Chen Y, Zhou J, Wang J, Liu W, Voogt J, Zhu X, Quan J, Li J (2013) Disaggregation of remotely sensed land surface temperature: literature survey, taxonomy, issues, and caveats. Remote Sens Environ 131:119–139

Zhao L, Lee X, Smith RB, Oleson K (2014) Strong contributions of local background climate to urban heat islands. Nature 511(7508):216–219

Zhao C, Jensen J, Weng Q, Weaver R (2018) A geographically weighted regression analysis of the underlying factors related to the surface urban heat island phenomenon. Remote Sens 10(9):1428

Zhou X, Chen H (2018) Impact of urbanization-related land use land cover changes and urban morphology changes on the urban heat island phenomenon. Sci Total Environ 635:1467–1476

Zhou D, Xiao J, Bonafoni S, Berger C, Deilami K, Zhou Y, Frolking S, Yao R, Qiao Z, Sobrino JA (2019) Satellite remote sensing of surface urban heat islands: progress, challenges, and perspectives. Remote Sens 11(1):48

Zhou B, Kaplan S, Peeters A, Kloog I, Erell E (2020) "Surface", "satellite" or "simulation": mapping intra-urban microclimate variability in a desert city. Int J Climatol 40(6):3099–3117